SLAC-PUB-15949

Quantum Spin Hall Insulator State in HgTe Quantum Wells

Markus König[1], Steffen Wiedmann[1], Christoph Brüne[1], Andreas Roth[1], Hartmut Buhmann[1], Laurens W. Molenkamp[1,*], Xiao-Liang Qi[2] and Shou-Cheng Zhang[2]

[1]Physikalisches Institut (EP III), Universität Würzburg
D-97074 Würzburg, Germany
[2]Department of Physics, McCullough Building, Stanford University
Stanford, CA 94305-4045
[*]To whom correspondence should be addressed:
molenkmp@physik.uni-wuerzburg.de

Recent theory predicted that the Quantum Spin Hall Effect, a fundamentally novel quantum state of matter that exists at zero external magnetic field, may be realized in HgTe/(Hg,Cd)Te quantum wells. We have fabricated such sample structures with low density and high mobility in which we can tune, through an external gate voltage, the carrier conduction from n-type to the p-type, passing through an insulating regime. For thin quantum wells with well width $d < 6.3$ nm, the insulating regime shows the conventional behavior of vanishingly small conductance at low temperature. However, for thicker quantum wells ($d > 6.3$ nm), the nominally insulating regime shows a plateau of residual conductance close to $2e^2/h$. The residual conductance is independent of the sample width, indicating that it is caused by edge states. Furthermore, the residual conductance is destroyed by a small external magnetic field.

Published in arXiv:0710.0582.

SIMES, SLAC National Accelerator Laboratory, 2575 Sand Hill Road, Menlo Park, CA 94025
Division of Materials Sciences and Engineering, under contract DE-AC02-76SF00515 and NSF.

The quantum phase transition at the critical thickness, $d = 6.3$ nm, is also independently determined from the magnetic field induced insulator to metal transition. These observations provide experimental evidence of the quantum spin Hall effect.

The theoretical prediction of the intrinsic spin Hall effect in metals and insulators (*1, 2, 3*) has generated great interests in the field of spintronics, since this effect allows for direct electric manipulation of the spin degrees of freedom without a magnetic field, and the resulting spin current can flow without dissipation. These properties could lead to promising spintronic devices with low power dissipation.

However, beyond the potential technological applications, the intrinsic spin Hall effect has guided us in the search for new and topologically non-trivial states of matter. The quantum Hall state gives the first, and so far the only example of a topologically non-trivial state of matter, where the quantization of the Hall conductance is protected by a topological invariant. The quantum spin Hall (QSH) insulators (*4, 5, 6*) have a similar, but distinct non-trivial topological property. The QSH insulators are invariant under time reversal, have a charge excitation gap in the bulk, but have topologically protected gapless edge states that lie inside the bulk insulating gap. This type of insulator is typically realized in spin-orbit coupled systems; the corresponding edge states have a distinct helical property: two states with opposite spin-polarization counter-propagate at a given edge (*4, 7, 8*). The edge states come in Kramers' doublets, and time reversal symmetry ensures the crossing of their energy levels at special points in the Brillouin zone. Because of this energy level crossing, the spectrum of a QSH insulator cannot be adiabatically deformed into that of a topologically trivial insulator without helical edge states; therefore, in this precise sense, the QSH insulators represent a topologically distinct new state of matter.

It has been proposed theoretically that HgTe/(Hg,Cd)Te quantum wells provide a natural realization of the quantum spin Hall effect (*6*). In zincblende-type semiconductor quantum wells, there are four relevant bands close to the Fermi level. The $E1$ band basically consists of the two spin states of the s orbital, while the $HH1$ band basically consists of the $|p_x + ip_y, \uparrow\rangle$ and $|-(p_x - ip_y), \downarrow\rangle$ orbitals. The effective Hamiltonian near the Γ point is given by

$$H_{eff}(k_x, k_y) = \begin{pmatrix} H(k) & 0 \\ 0 & H^*(-k) \end{pmatrix}, \quad H = \epsilon(k) + d_i(k)\sigma_i \tag{1}$$

where σ_i are the Pauli matrices, and

$$d_1 + id_2 = A(k_x + ik_y) \equiv Ak_+$$
$$d_3 = M - B(k_x^2 + k_y^2)\ ,\ \epsilon_k = C - D(k_x^2 + k_y^2). \tag{2}$$

Here, k_x and k_y are momenta in the plane of the 2DEG, while A, B, C, D are material specific constants. Spin-orbit coupling is naturally built-in in this Hamiltonian through the spin-orbit coupled p orbitals $|p_x + ip_y, \uparrow\rangle$ and $|-(p_x - ip_y), \downarrow\rangle$. Two dimensional materials can be grouped into three types according to the sign of the Dirac mass parameter M. In conventional semiconductors such as GaAs and CdTe, the s-like $E1$ band lies above the p-like $HH1$ band, and the mass parameter M is positive. Semi-metals such as graphene (*9, 10*) are described by a massless Dirac model with $M = 0$, although the bands have a different physical interpretation. In so-called "inverted" semiconductors such as HgTe, the s-like orbital lies below the p-like orbitals; therefore, the Dirac mass parameter M in the HgTe/(Hg,Cd)Te quantum wells can be continuously tuned from a positive value $M > 0$ for thin quantum wells with thickness $d < d_c$ to a negative value $M < 0$ for thick quantum wells with $d > d_c$. A topological quantum phase transition occurs at $d = d_c$, where the system is effectively described by a massless Dirac theory just like for graphene. The nature of this quantum phase transition has also been investigated in more realistic models beyond the simple four band model presented here, reaching the same conclusion (*11*).

The QSH phase occurs in the inverted regime where $M < 0$, i.e., when $d > d_c$. The sample edge can be viewed as a domain wall of the mass parameter M, separating the topologically non-trivial phase with $M < 0$ from the topologically trivial phase with $M > 0$, which is adiabatically connected to the vacuum (*12*). Massless helical states are confined on the sample edge. The sample has a finite conductance even when the Fermi level lies inside the bulk insulating gap. Therefore, as suggested in Ref. 6, the QSH state can be experimentally detected by mea-

suring a residual conductance plateau as one varies the gate voltage in the nominally insulating regime. Furthermore, because the current is carried by the edge states, the conductance should be independent of sample width. Protected by the time reversal symmetry, non-magnetic impurities or any other time-reversal invariant local perturbations cannot cause elastic backscattering of the helical edge states, which warrants the topological robustness of the edge state conductance. However, the presence of magnetic field breaks time reversal symmetry, therefore can open up a gap in the energy spectrum of the edge states, and remove the residual conductance due to the edge states.

We set out to test these theoretical predictions by measuring the transport properties of HgTe/(Hg,Cd)Te quantum wells as a function of the sample thickness, the gate voltage and the external magnetic field. We use modulation-doped type-III (*13*) HgTe/$Hg_{0.3}Cd_{0.7}$Te quantum well (QW) structures fabricated by molecular beam epitaxy (*14*), with widths (*15*) varying from 5.5 nm ($d < d_c$) to 12 nm ($d > d_c$). Dedicated low-thermal budget optical and e-beam lithography is used to structure devices in Hall bar geometry with dimensions, $(L \times W)$, of (600×200) μm^2, (20.0×13.3) μm^2, (1.0×1.0) μm^2, and (1.0×0.5) μm^2 (see inset in Fig. 1A). All devices have a 110 nm thick Si_3N_4/SiO_2 multilayer gate insulator (*16*) and a 5/30 nm Ti/Au gate electrode stack. Transport measurements are done in a ^{3}He/^{4}He-dilution refrigerator (base temperature $T < 30$ mK, uniaxial fields up to 18 T) and in a ^{4}He cryostat fitted with a vector magnet ($T = 1.4$ K, and fields up to 300 mT in variable direction), using lock-in techniques. At zero gate voltage, the samples are n-type, exhibiting carrier densities between 1.3×10^{11} cm^{-2} and 3.5×10^{11} cm^{-2} and mobilities up to 1.5×10^5 cm^2/(Vs). The carrier density can be reduced continuously by applying a negative gate voltage to the Au electrode with respect to carriers in the QW. The Si-O-N gate insulator stack allows for quite large gate voltages, enabling us to gate the samples through the gap from n-type to p-type conductance.

The change in carrier type can be monitored from Hall experiments, as shown in Fig. 1A

for a large $[(L \times W) = (600 \times 200)\ \mu\mathrm{m}^2]$ Hall bar with a well width of 6.5 nm, at 30 mK. The change in carrier type is directly reflected in a sign change of the slope of the Hall resistance R_{xy}, and we can directly infer that the carrier density varies from $n = 1.2 \times 10^{11}$ cm^{-2} at gate voltage V_g = -1.0 V to $p = 1.0 \times 10^{10}$ cm^{-2} at V_g = -2.0 V. At modest magnetic fields, for both n-type and p-type channels, R_{xy} exhibits quantum Hall plateaus, indicative of the good quality of the material, until at fields above ca. 3 T the last Landau level is depleted.

Remarkable transport behavior is observed for -1.9 V $\leq V_g \leq$ -1.4 V (see in particular the green and the red traces in Fig. 1), where the sample is insulating at zero magnetic field (i.e., the Fermi level is in the gap). For these gate voltages, we observe that the sample undergoes a phase transition from an insulating state to a QH state with a quantized Hall conductance of $G_{xy} = \pm e^2/h$, either n- or p-type depending on V_g, at a small (order 1-2 T) applied magnetic field. The sample remains in the QH state for a few more T, and then becomes once again insulating. We have observed this phenomenon in a number of samples in the inverted regime, with 6.5 nm $< d <$ 12 nm.

The phase transition from an insulating state to a QH state is a non-trivial consequence of the inverted band structure of the QSH insulator, and can be explained by the level crossing of the $E1$ and $HH1$ Landau levels, which can be directly obtained from the minimal coupling of the simple Dirac model Eq. 1 to a perpendicular magnetic field $B_\perp$. If we only consider the orbital effects of the magnetic field, two series of Landau levels are obtained from the upper and lower 2×2 blocks of Hamiltonian, Eq. 1, in which the two levels closest to the Fermi energy are given by $E_+ = C + M - (D + B)l_c^{-2}$ and $E_- = C - M - (D - B)l_c^{-2}$, with $l_c \equiv \sqrt{\hbar/(eB_\perp)}$. Thus the condition for level crossing is given by $E_+ - E_- = 2M - 2Bl_c^{-2} = 0$ or $B_\perp^c = (\hbar M)/(eB)$. Generally, the B parameter is always negative, therefore, we can see that the level crossing occurs only in the inverted region with $M < 0$.

The Landau levels for the normal ($d < d_c$) and the inverted ($d > d_c$) regime are shown

in Fig. 2A and B, respectively. Edge states in the presence of an external magnetic field can be easily obtained by solving our simple Dirac model in Eq. 1 with open boundary condition along one direction and periodic boundary condition along the other direction. Fig. 2C shows the bulk and edge states for a conventional insulator. With increasing thickness d, the two states closest to the Fermi energy approach and then cross each other. This "band inversion" leads to the bulk and edge states [Fig. 2D]. The Fermi energy crosses a pair of counter-propagating edge states on each edge, resulting in no net Hall effect. These counter-propagating edge states are similar to the helical edge states of the QSH insulator. However, due to the presence of the magnetic field and the breaking of the time reversal symmetry, they are not robustly protected. Starting from this case, increasing magnetic field shifts the red Landau level towards higher and the blue one towards lower energies. When one of the bulk Landau level crosses the Fermi level, there is a single edge state on each edge left, and one obtains a net QH effect with either $G_{xy} = e^2/h$ [Fig. 2E], or with $G_{xy} = -e^2/h$ [Fig. 2F]. When the magnetic field is increased further, the second bulk Landau level crosses the Fermi level, and one reaches the conventional insulator case [Fig. 2C] but with the colors of the Landau level interchanged. In models with bulk inversion asymmetry (BIA) (*11*), the level crossing between $E1$ and $HH1$ Landau levels at $B_{\perp}^{c}$ can be avoided, and the phase regions (i) and (ii) in Fig. 2B become connected. Generally, the non-monotonic dependence of the Landau level energies leads to the transition from the insulating state to the QH state at a constant Fermi energy, when the magnetic field is varied.

While the four band Dirac model (Eq. 1) gives a simple qualitative understanding of this novel phase transition, we have also performed more realistic and self-consistent eight band $\mathbf{k} \cdot \mathbf{p}$ model calculations (*13*) for a 6.5 nm quantum well, with the fan chart of the Landau levels displayed in Fig. 1B. The two anomalous Landau levels cross at a critical magnetic field $B_{\perp}^{c}$, which evidently depends on well width. This implies that when a sample has its Fermi energy in the gap at zero magnetic field, this energy will always be crossed by the two anomalous

Landau levels, resulting in a QH plateau in between the two crossing fields. Fig. 3 summarizes the dependence of $B_\perp^c$ on well width d. The open red squares are experimental data points that result from fitting the 8-band $\mathbf{k} \cdot \mathbf{p}$ model to experimental data as in Fig. 1, while the filled red triangles solely result from the $\mathbf{k} \cdot \mathbf{p}$ calculation. For reference, the calculated gap energies are also plotted in this graph as open blue circles. The band inversion is reflected in the sign change of the gap. Note that for relatively wide wells ($d > 8.5$ nm) the (inverted) gap starts to decrease in magnitude. This is because for these well widths, the band gap no longer occurs between the $E1$ and $HH1$ levels, but rather between $HH1$ and $HH2$ - the second confined hole-like level, as schematically shown in the inset of Fig. 3 [see also (*17*)]. Also in this regime, a band crossing of conductance- ($HH1$) and valence- ($HH2$) band derived Landau levels occurs with increasing magnetic field (*13, 17, 18*). Fig. 3 clearly illustrates the quantum phase transition that occurs as a function of d in the HgTe QWs: only for $d > d_c$, $B_\perp^c$ exists, and at the same time the energy gap is negative (i.e., the band structure is inverted). The experimental data allow for a quite accurate determination of the critical thickness, yielding $d_c = 6.3 \pm 0.1$ nm.

The actual existence of edge channels in insulating inverted QWs is only revealed when studying smaller Hall bars (note that the typical mobility of 10^5 cm^2/(Vs) in n-type material implies an elastic mean free path of $l_{\rm mfp} \approx 1$ μm (*19, 20*) - and one may anticipate lower mobilities in the nominally insulating regime). The pertinent data is shown in Fig. 4, which plots the zero B-field four terminal resistance $R_{14,23} \equiv V_{23}/I_{14}$ as a function of normalized gate voltage (V_{thr} is defined as the voltage for which the resistance is largest) for several devices, that are representative for the large number of structures we have investigated. $R_{14,23}$ is measured while the Fermi level in the device is scanned through the gap. In the low resistance regions at positive $V_g - V_{thr}$ the sample is n-type, at negative $V_g - V_{thr}$ the sample is p-type.

The black curve labeled I in Fig. 4 is obtained from a medium sized [(20.0×13.3) μm^2] device with 5.5 nm QW, and shows the behavior we observe for all devices with a normal band

structure: when the Fermi level is in the gap, $R_{14,23}$ increases strongly and is at least several tens of MΩ (this actually is the noise floor of the lock-in equipment used in the experiment). This clearly is the expected behavior for a conventional insulator. However, for all devices containing an inverted QW, the resistance in the insulating regime remains finite. $R_{14,23}$ plateaus out at well below 100 kΩ (i.e., $G_{14,23} = 0.3e^2/h$) for the blue curve labeled II, which is again for a (20.0×13.3) μm^2 device fabricated by optical lithography, but now contains a 7.3 nm wide QW. For much shorter samples ($L = 1.0$ μm, green and red curves III and IV) fabricated from the same wafer, $G_{14,23}$ actually reaches the predicted value close to $2e^2/h$. This observation provides firm evidence for the existence of the quantum spin Hall insulator state for inverted HgTe QW structures.

In Fig. 4, we have included data on two $d = 7.3$ nm, $L = 1.0$ μm devices. The green trace (III) is from a device with $W = 1.0$ μm, the red trace (IV) corresponds to $W = 0.5$ μm. Clearly, the residual resistance of the devices does not depend on the width of the structure, which is evidence that the transport occurs through edge channels (*21*). One notices that the traces for the $d = 7.3$ nm, $L = 1.0$ μm devices do not reach all the way into the p-region. This is because the electron-beam lithography needed to fabricate the devices increases the intrinsic ($V_g = 0$ V) carrier concentration. In addition, one notices fluctuations on the conductance plateaus in traces II, III, and IV. These fluctuations are actually reproducible and do not stem from, e.g., electrical noise. While all $R_{14,23}$ traces discussed so far were taken at base temperature (30 mK) of our dilution refrigerator, the conductance plateaus are not at all limited to this very low temperature regime. In the inset of Fig. 4 we reproduce the green 30 mK trace III on a linear scale, and compare it with a trace (in black) taken at 1.8 K from another $(L \times W) = (1.0 \times 1.0)$ μm^2 sample, that was fabricated from the same wafer. In the fabrication of this sample, we used a lower illumination dose in the e-beam lithography, resulting in a better (but still not quite complete) coverage of the n-i-p transition. Clearly, in this further sample, and at 1.8

K, the $2e^2/h$ conductance plateau is again present, including (thermally smeared) conductance fluctuations.

In the pure two terminal geometry, with only source and drain contacts (contacts 1 and 4, inset Fig 1A), the two counter propagating helical edge states at one given edge connect the chemical potential from the source and drain, respectively, and they are not in equilibrium with each other because the elastic backscattering vanishes between these two channels. In the absence of voltage probes 2,3,5, and 6, as indicated in the inset of Fig. 1, the two terminal conductance should give $2e^2/h$. Now we consider the presence of the voltage probes. Since our voltage probes are not spin sensitive, the voltage measurement necessarily leads to the equilibration of the two helical channels with the opposite spin orientation. A simple Landauer-Büttiker type of calculation shows that the four terminal resistance should in fact be given by $R_{14,23} = h/2e^2$. In the presence of the voltage probes, the voltage drops V_{12}, V_{23} and V_{34} add in series to give a higher resistance of $R_{14} \equiv V_{14}/I_{14} = 3h/2e^2$. These results are valid as long as the distance between the voltage probes is less than the inelastic mean free path l_{in}. While elastic scatterers can not cause backscattering of the helical edge states, inelastic scatterers can. We estimate the inelastic mean free path to be $l_{in} > 1\mu m$ at our measurement temperature. Therefore, for the large sample (II), where the distance between the voltage probes exceeds the inelastic mean free path l_{in}, we expect the residual resistance to be higher, consistent with the experimental measurement shown in the trace (II) in Fig. 4.

Another intriguing observation is that the QSH effect is destroyed by applying only a small magnetic field perpendicular to the 2DEG plane. Fig. 5 shows that the magnetoresistance is actually strongly anisotropic. (This data has been obtained in the vector magnet system at 1.4 K.) A very sharp, cusp-like conductance peak is observed for perpendicular field, with the full width half-maximum (FWHM) $B_{\perp}^{FWHM} \simeq 28$ mT (*22*). The peak broadens strongly when the magnetic field is tilted into the QW plane. For fully in-plane fields, the QSH conductance can

be observed over a much wider magnetic field range ($B_{\parallel}^{\mathrm{FWHM}} \approx 0.7$ T).

The robustness of the helical edge states is ensured by the time-reversal symmetry. A magnetic field breaks time reversal symmetry, and thus turns on a gap between the two otherwise degenerate helical edge states. The perpendicular and in-plane magnetic field lead to different gaps, depending on the matrix elements of the magnetization operator:
$E_{\mathrm{gap}\perp} = \langle\uparrow| \left(\hat{\mathbf{z}} \cdot \hat{\mathbf{r}} \times \hat{\mathbf{j}} + g_{\perp}\mu_B S_{\perp}\right) |\downarrow\rangle |B|$ and $E_{\mathrm{gap}\parallel} = \langle\uparrow| g_{\parallel}\mu_B S_{\parallel} |\downarrow\rangle |B|$, in which $\hat{\mathbf{r}}, \hat{\mathbf{j}}$ are the position and electric current operator, respectively, and $\hat{\mathbf{z}}$ is the unit-vector perpendicular to the quantum well plane. $S_{\perp(\parallel)}$ stands for the dimensionless part of the Zeeman-coupling matrix element in perpendicular (parallel) magnetic field. We can estimate the magnitude of these two gaps by noting that $\langle\uparrow| \hat{\mathbf{z}} \cdot \hat{\mathbf{r}} \times \hat{\mathbf{j}} |\downarrow\rangle \sim ev\xi$ and $\langle\uparrow| S_{\parallel,\perp} |\downarrow\rangle \sim 1$, in which v and ξ are the Fermi velocity and width of the edge channels, respectively. v and ξ can be obtained from the Dirac parameters as $v = A/\hbar$ and $\xi \simeq \hbar v/|M|$. The parameters for the $d = 7.3$ nm quantum well give the dimensionless ratio $ev\xi/\mu_B \sim 280$, which thus leads to $E_{\mathrm{gap}\perp}/E_{\mathrm{gap}\parallel} \sim 10^2$. From this estimate, we can see that the strong anisotropy observed in the experiments originates from the high Fermi velocity of the edge states and the small bulk gap M, which together make the orbital magnetization dominant.

So far our experiments have only measured the charge transport properties. While the QSH effect manifests itself already in the change in transport properties, we would still like to experimentally confirm the spin accumulation resulting from the spin Hall effect (*23, 24*) in the topologically non-trivial insulating regime, and compare both electric and magnetic results with the experiments of the spin Hall effect in the metallic regime. It would also be interesting to explore the regime close to the quantum phase transition point of $d = d_c$, and compare the transport properties with that of the recently discovered graphene. In many ways, the HgTe quantum well system can be viewed as a tunable graphene system, where the Dirac mass term can be tuned continuously to zero from either the positive (topologically trivial) or the negative

(topologically non-trivial) side.

References and Notes

1. S. Murakami, N. Nagaosa, S.C. Zhang, *Science* **301**, 1348 (2003).

2. J. Sinova, *et al.*, *Phys. Rev. Lett.* **92**, 126603 (2004).

3. S. Murakami, N. Nagaosa, S.C. Zhang, *Phys. Rev. Lett.* **93**, 156804 (2004).

4. C. L. Kane, E. J. Mele, *Phys. Rev. Lett.* **95**, 146802 (2005).

5. B.A. Bernevig, S.C. Zhang, *Phys. Rev. Lett.* **96**, 106802 (2006).

6. B. A. Bernevig, T. L. Hughes, S.C. Zhang, *Science* **314**, 1757 (2006).

7. C. Wu, B.A. Bernevig, S.C. Zhang, *Phys. Rev. Lett.* **96**, 106401 (2006).

8. C. Xu, J. Moore, *Phys. Rev. B* **73**, 045322 (2006).

9. K. S. Novoselov, *et al.*, *Nature* **438**, 197 (2005).

10. Y. Zhang, Y. Tan, H. L. Stormer, P. Kim, *Nature* **438**, 201 (2005).

11. X. Dai, T. L. Hughes, X. Qi, Z. Fang, S. Zhang, arxiv: cond-mat/0705.1516.

12. Similar mass domain walls have been proposed to occur in three-dimensional in PbTe/(Pb,Sn)Te heterostructures, where the $L_6^{\pm}$ bands change position as a function of Sn concentration (*25, 26*).

13. E. G. Novik, *et al.*, *Phys. Rev. B* **72**, 035321 (2005).

14. C. Becker, *et al.*, *Phys. Stat. Sol. (c)* **4**, 3382 (2007).

15. Well thicknesses have been calibrated using X-Ray Reflectivity measurements at the DESY synchrotron in Hamburg, Germany.

16. J. Hinz, *et al.*, *Semicond. Sci. Technol.* **21**, 501 (2006).

17. A. Pfeuffer-Jeschke, Ph.D. Thesis, University of Würzburg, Germany, 2000.

18. M. Schultz, *et al.*, *Phys. Rev. B* **57**, 14772 (1998).

19. V. Daumer, *et al.*, *Appl. Phys. Lett.* **83**, 1376 (2003).

20. M. König, *et al.*, *Phys. Rev. Lett.* **96**, 76804 (2006).

21. We have actually observed a similar independence of resistance on sample width in the $d =$7 nm, $L = 20.0$ μm devices, showing that also in these larger structures the conductance is totally dominated by edge channels.

22. FWHM of the magnetoresistance peak is about 10 mT at 30 mK, increasing to 28 mT at 1.4 K.

23. Y. K. Kato, R. C. Myers, A. C. Gossard, D. D. Awschalom, *Science* **306**, 1910 (2004).

24. J. Wunderlich, B. Kaestner, J. Sinova, T. Jungwirth, *Phys. Rev. Lett.* **94**, 047204 (2005).

25. B. A. Volkov, O. A. Pankratov, *JETP Lett.* **42**, 178 (1985).

26. E. Fradkin, E. Dagotto, D. Boyanovsky, *Phys. Rev. Lett.* **57**, 2967 (1986).

27. We wish to thank A. Bernevig, X. Dai, Z. Fang, T. Hughes, C. X. Liu and C.J. Wu for insightful discussions, C.R. Becker and V. Hock for sample preparation, and C. Kumpf for calibrating the well widths of the HgTe samples. This work is supported by the DFG (SFB 410), by the German-Israeli Foundation for Scientific Research and Development (Grant No.881/05), by NSF through the grants DMR-0342832, and by the US Department of Energy, Office of Basic Energy Sciences under contract DE-AC03-76SF00515, and Focus Center Research Program (FCRP) Center on Functional Engineered Nanoarchitectonics (FENA).

1 Figure Captions

Fig. 1 (A) Hall resistance, R_{xy}, of a $(L \times W) = (600 \times 200)$ μm^2 QW structure with 6.5 nm well width for different carrier concentrations obtained for gate voltages V_g of -1.0 V (black), -1.1 V (purple), -1.2 V (navy), -1.3 V (blue), -1.35 V (cyan), -1.4 V (green), -1.7 V (red), -1.8 V (orange), -1.9 V (brown), and -2.0 V (black, lower curve). For decreasing V_g, the n-type carrier concentration decreases and a transition to a p-type conductor is observed, passing through an insulating regime between -1.4 and -1.9 V at $B = 0$ T. The inset shows a schematic sample layout with ohmic contacts labeled 1 to 6. The grey shaded region indicates the top gate electrode and defines the part of the sample where the carrier concentration and type can be changed. Red and blue arrows indicate the counter-propagating spin-polarized edge channels of the QSH effect. (B) The Landau level fan chart of a 6.5 nm quantum well obtained from an eight band $\mathbf{k} \cdot \mathbf{p}$ calculation. Black dashed lines indicate the energetic position of the Fermi energy, E_F, for $V_g = -1.0$ and -2.0 V. Red and green dashed lines correspond to position of the Fermi energies of the red and green Hall resistance traces of Fig. A. The Landau level crossing points are marked by arrows of the same color.

Fig. 2 Bulk and edge state spectrum of the four band Dirac model described by Eq. 1 in the presence of an external orbital magnetic field. (A) The bulk Landau levels in the normal regime. (B) The bulk Landau levels in the inverted regime. A pair of low lying Landau levels cross at a finite magnetic field $B_\perp^c$. The crossing divides the phase diagram of gate voltage and magnetic field into four regimes, labelled (i-iv) in the figure. (C) The low lying bulk and edge state energies as a function of the centers of the Landau orbitals in the normal regime. (D) The low lying bulk and edge state energies as a function of the centers of the Landau orbitals for the inverted regime, where the Fermi energy lies in between the two bulk inverted Landau levels. The Fermi energy crosses the Landau levels, giving rise to the one pair of counter-propagating

edge states. When the magnetic field is increased, the two lowest lying bulk Landau levels approach each other, and they cross the Fermi energy in different order, depending on the value of the gate voltage. The crossing of the Fermi energy by one of the Landau levels gives rise to either the $n-$ or the p-type QHE for the cases shown in figures (E) and (F).

Fig. 3 Crossing field, $B_{\perp}^{c}$, (red triangles) and energy gap, E_g, (blue open dots) as a function of QW width d resulting from an eight band $\mathbf{k} \cdot \mathbf{p}$ calculation. For well widths larger than 6.3 nm the QW is inverted and a mid-gap crossing of Landau levels deriving from the $HH1$ conductance and $E1$ valence band occurs at finite magnetic fields. The experimentally observed crossing points are indicated by open red squares. The inset shows the energetic ordering of the QW subband structure as a function of QW width d. [taken from Ref. (*17*)]

Fig. 4 The longitudinal four-terminal resistance, $R_{14,23}$, of various normal ($d = 5.5$ nm) (I) and inverted ($d = 7.3$ nm) (II, III, and IV) QW structures as a function of the gate voltage measured for $B = 0$ T at $T = 30$ mK. The device sizes are (20.0×13.3) μm^2 for device I and II, (1.0×1.0) μm^2 for device III, and (1.0×0.5) μm^2 for device IV. The inset shows $R_{14,23}(V_g)$ of two samples from the same wafer, having the same device size (III) at 30 mK (green) and 1.8 K (black) on a linear scale.

Fig. 5 Four-terminal magnetoconductance, $G_{14,23}$, in the QSH regime as a function of tilt angle between the plane of the 2DEG and applied magnetic field for a $d = 7.3$ nm QW structure with dimensions $(L \times W) = (20 \times 13.3)$ μm^2 measured in a vector field cryostat at 1.4 K.

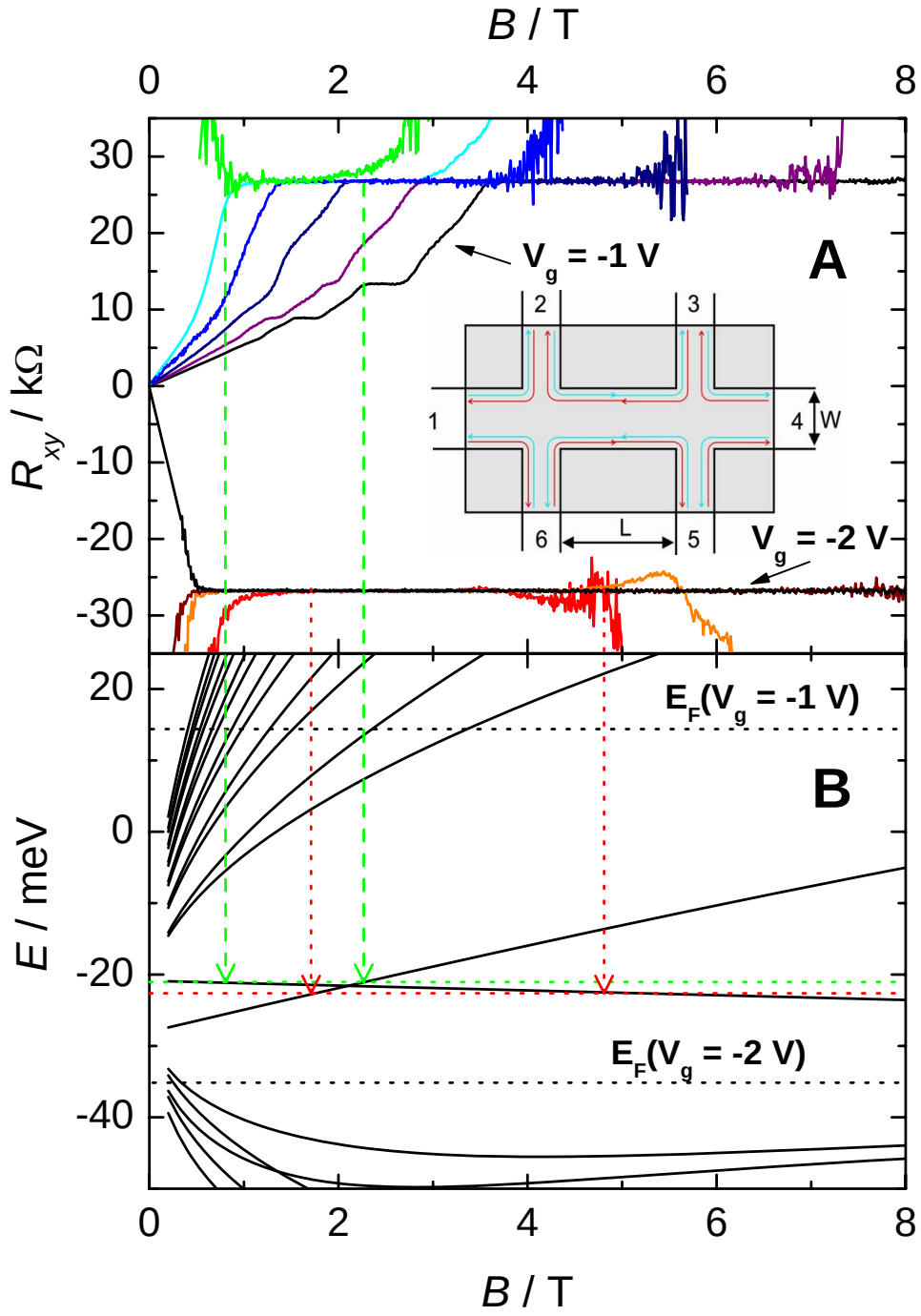
B / T
0
2
4
6
8
30
20
10
0
-10
-20
-30
R_xy / kΩ
V_g = -1 V
A
2
3
1
4
W
6
L
5
V_g = -2 V
20
0
-20
-40
E / meV
E_F(V_g = -1 V)
B
E_F(V_g = -2 V)
B / T

Fig. 1

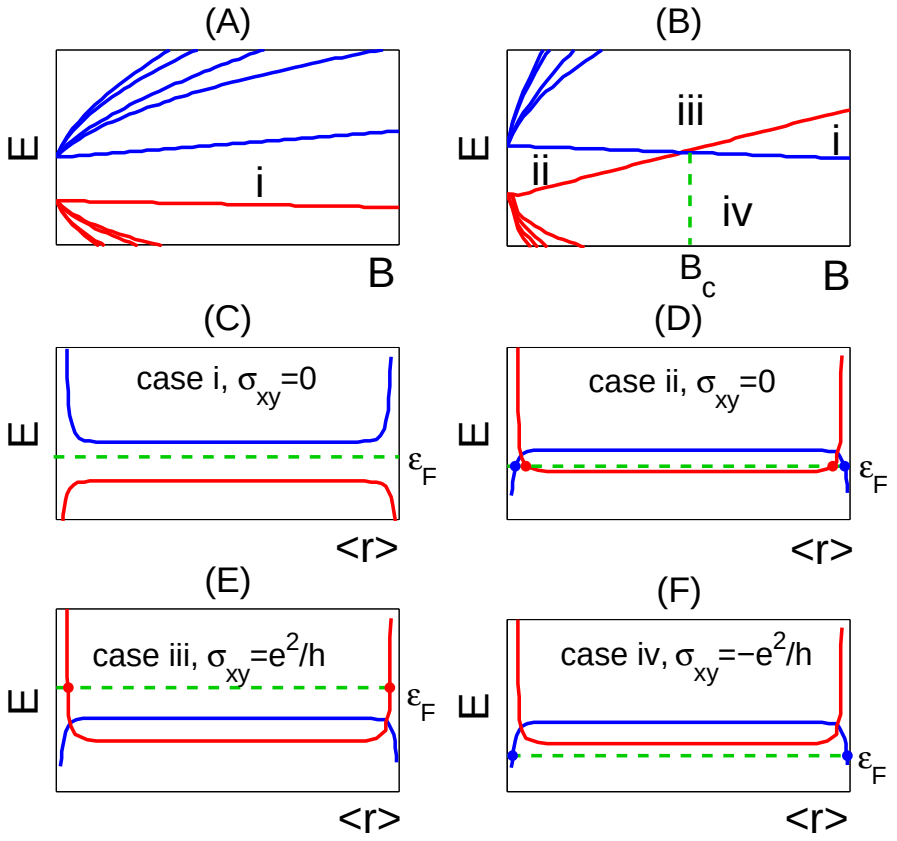
(A)
E
i
B
(B)
E
iii
i
ii
iv
B_c
B
(C)
E
case i, σ_xy=0
ε_F
<r>
(D)
E
case ii, σ_xy=0
ε_F
<r>
(E)
E
case iii, σ_xy=e^2/h
ε_F
<r>
(F)
E
case iv, σ_xy=−e^2/h
ε_F
<r>

Fig. 2

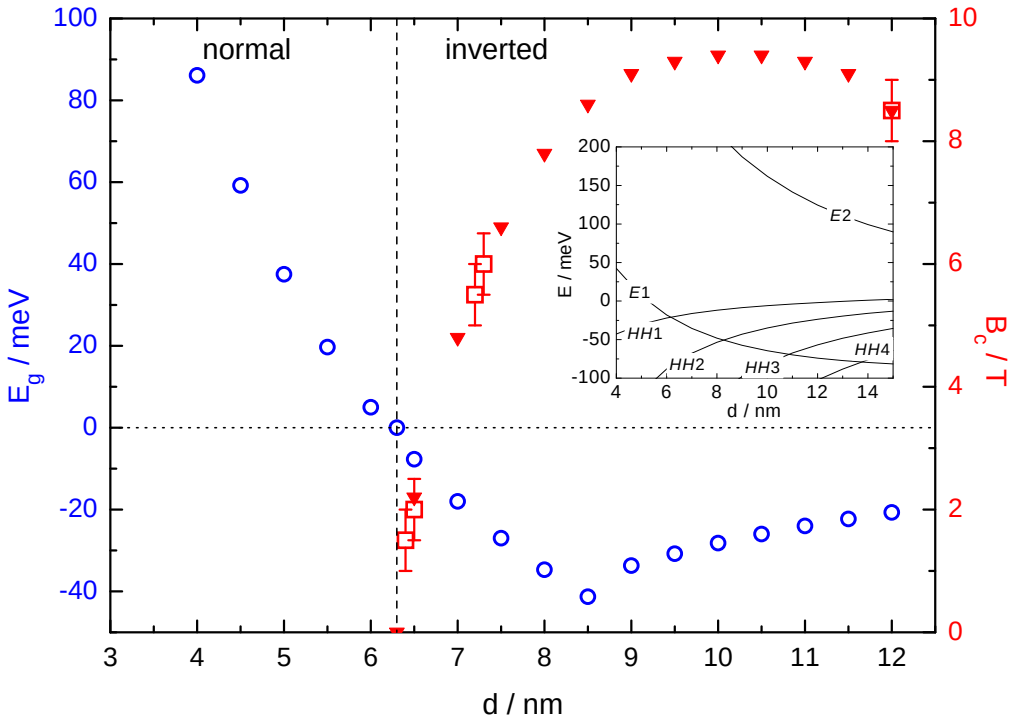

Fig. 3

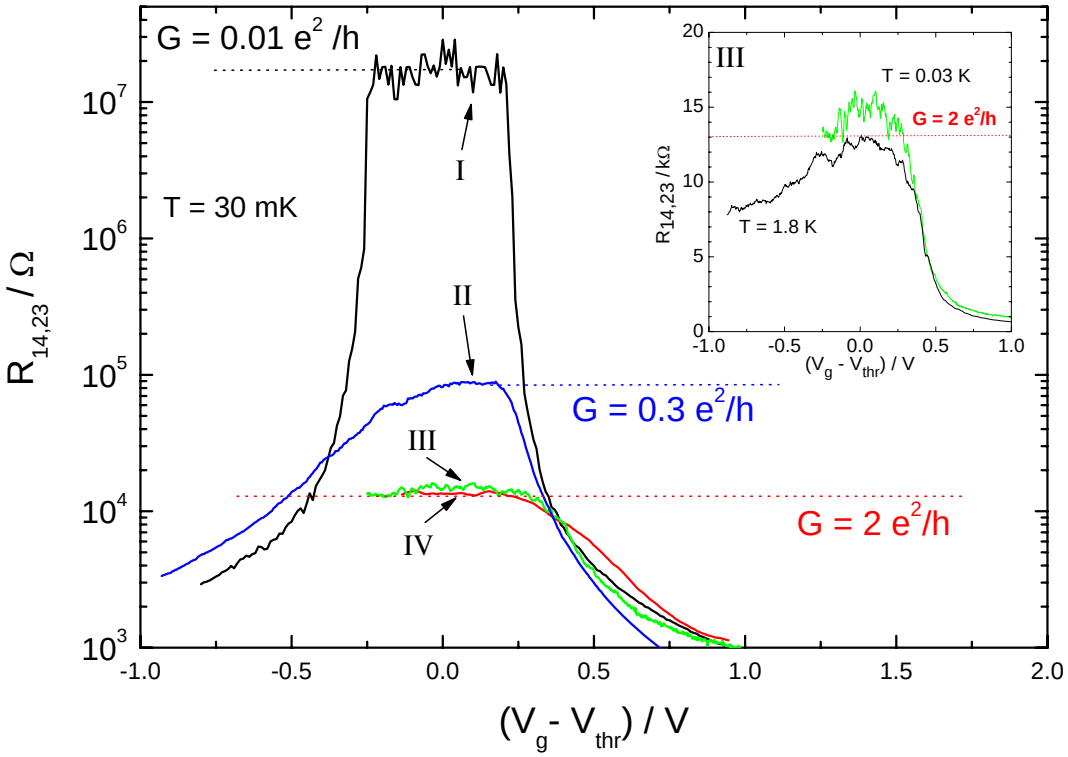
G = 0.01 e2 /h
T = 30 mK
I
II
III
IV
G = 0.3 e2/h
G = 2 e2/h
R14,23 / Ω
(Vg - Vthr) / V
III
T = 0.03 K
G = 2 e2/h
T = 1.8 K
R14,23 / kΩ
(Vg - Vthr) / V

Fig. 4

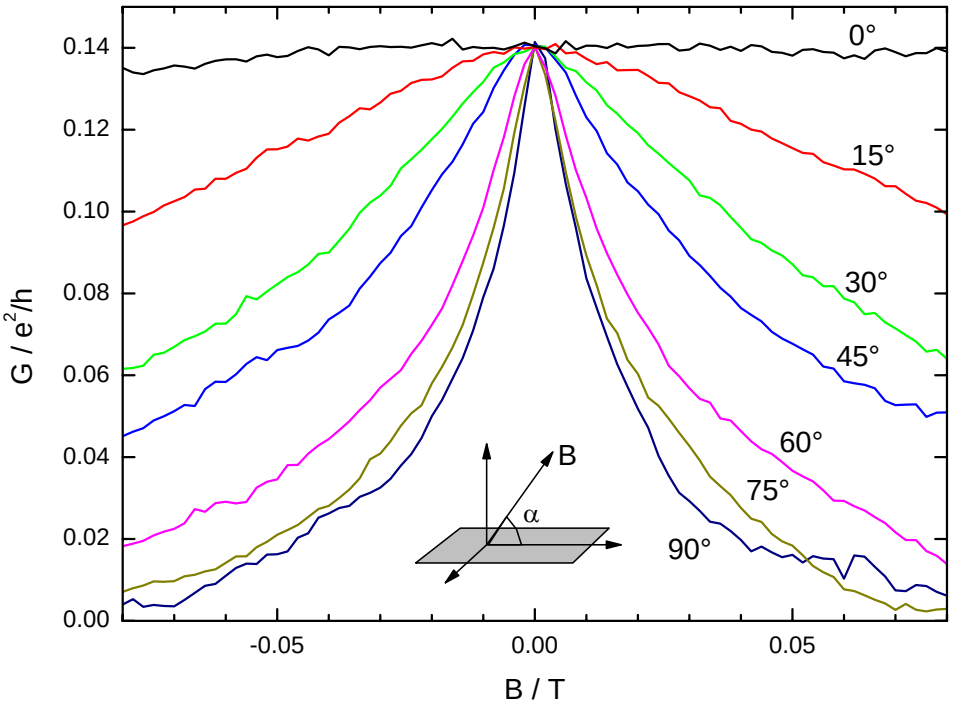
0°
15°
30°
45°
60°
75°
90°
B
α
G / e²/h
B / T
0.14
0.12
0.10
0.08
0.06
0.04
0.02
0.00
-0.05
0.00
0.05

Fig. 5